Printable Block Molecular Assemblies with Controlled Exciton Dynamics

Zongshang Li, Jihyuk Yang, Fengke Sun, Kam-Hung Low, Wenming Tian, Shengye Jin, Ji Tae Kim, Chi-Ming Che,* and Qingyun Wan*

Creating hierarchical molecular block heterostructures, with the control over size, shape, optical, and electronic properties of each nanostructured building block can help develop functional applications, such as information storage, nanowire spectrometry, and photonic computing. However, achieving precise control over the position of molecular assemblies, and the dynamics of excitons in each block, remains a challenge. In the present work, the first fabrication of molecular heterostructures with the control of exciton dynamics in each block, is demonstrated. Additionally, these heterostructures are printable and can be precisely positioned using Direct Ink Writing-based (DIW) 3D printing technique, resulting in programable patterns. Singlet excitons with emission lifetimes on nanosecond or microsecond timescales and triplet excitons with emission lifetimes on millisecond timescales appear simultaneously in different building blocks, with an efficient energy transfer process in the heterojunction. These organic materials also exhibit stimuli-responsive emission by changing the power or wavelength of the excitation laser. Potential applications of these organic heterostructures in integrated photonics, where the versatility of fluorescence, phosphorescence, efficient energy transfer, printability, and stimulus sensitivity co-exist in a single nanowire, are foreseen.

1. Introduction

Rational design and synthesis of heterostructures with different functional building blocks is a critical step in the fabrication of nanoscale or microscale integrated organic optoelectronics.[1] Organic heterostructures were demonstrated to have wide applications in photonic logic gate devices, photonic transistors, optical routers and modulators, field effect transistors, and others.[1c,2] For light-emitting organic heterostructures, good control over the emission color from the visible to the near-infrared spectral region has been achieved and reported.[3] However, control of emission lifetimes and exciton dynamics in different time regimes (from nanoseconds to microseconds) has not yet been achieved in the construction of organic heterostructures.[1a,b] Singlet excitons and triplet excitons have different photophysical characteristics in terms of emission lifetime, exciton diffusion, exciton-exciton annihilation, and energy transfer mechanisms (Föster energy transfer for singlet excitons and Dexter energy transfer for triplet excitons). We envision that organic heterostructures composed of blocks with singlet or triplet excitons will yield intriguing photo-physical properties. These heterostructures may find various optoelectronic applications related to light harvesting, energy transfer, and others.[2c] For the preparation of molecular heterostructures, several methods have been developed in the literature, including living supramolecular polymerization,[4] crystallization-driven self-assembly,[5] and others.[1a,b] Nonetheless, precise control over the position and location of molecular assemblies is difficult to achieve but is important for the fabrication of integrated organic optoelectronics.

Z. Li, J. Yang, K.-H. Low, C.-M. Che, Q. Wan
Department of Chemistry
State Key Laboratory of Synthetic Chemistry
HKU-CAS Joint Laboratory on New Materials
The University of Hong Kong
Pokfulam Road, Hong Kong China
E-mail: cmche@hku.hk; qywan@connect.hku.hk

F. Sun, W. Tian, S. Jin
State Key Laboratory of Molecular Reaction Dynamics and Dynamics
Research Center for Energy and Environmental Materials
Dalian Institute of Chemical Physics
Chinese Academy of Sciences
Dalian 116023, China
J. T. Kim
Department of Mechanical Engineering
The University of Hong Kong
Pokfulam Road, Hong Kong China
C.-M. Che
HKU Shenzhen Institute of Research & Innovation
Shenzhen 518057, China
C.-M. Che
Hong Kong Quantum AI Lab Limited Units 909–915
Building 17W, 17 Science Park West Avenue, Pak Shek Kok, Hong Kong China

**ADVANCED
SCIENCE NEWS**

www.advancedsciencenews.com
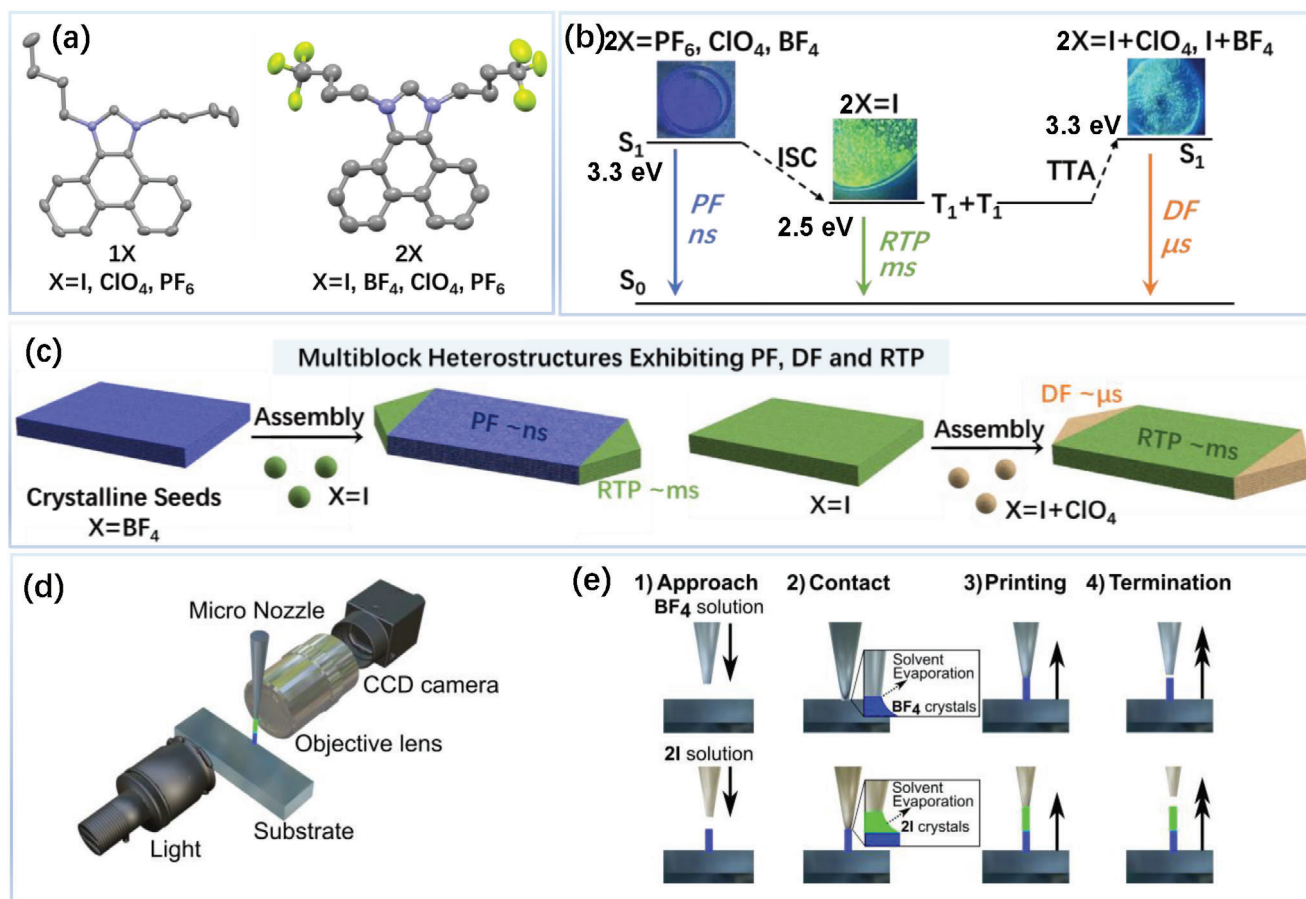
**ADVANCED
MATERIALS**

www.advmat.de

Figure 1. a) Crystal structures of compound **1** and **2**. Grey atom: C, blue atom: N, yellow-green atom: F. H atoms were not shown here for clarity. b) Scheme showing PF, RTP and DF of compound **2** obtained by changing the counteranions, and photographs of the crystals upon photo-excitation (λ_{ex} = 365 nm). The energy level of the S_1 and T_1 states of compound **2** are determined by the 0-0 transition energies measured by time-resolved PL spectroscopy. TTA: triplet-triplet annihilation, ISC: intersystem crossing. c) Scheme of preparing organic heterostructures by crystallization-driven self-assembly method. d) Schematic diagram of the 3D printing platform, including the moving part of the micro nozzle and substrate controlled by the assembled motorized stages, and the observation part with objective lens and CCD camera that collects the transmitted light. e) Schematic of the two-step printing process for **2BF$_4$** and **2I** diblock heterostructures (The arrow indicates the movement direction of the micro nozzle).

In the present work, we use metal-free imidazole cationic molecules as building blocks to fabricate various organic heterostructures (**Figure 1a**). By simply adjusting the counteranion of I^-, PF_6^-, ClO_4^- or BF_4^-, imidazole crystals can display short-lived prompt fluorescence (PF) with a lifetime as low as nanoseconds, or delayed fluorescence (DF) with a lifetime on the order of microseconds, or long-lived room temperature phosphorescence (RTP) with a lifetime up to milliseconds (Figure 1b).[6,7] By utilizing crystallization-driven self-assembly methods, we fabricated a series of heterostructures composed of light-emitting PF, DF, or RTP building blocks (Figure 1c). To the best of our knowledge, the molecular heterostructures prepared and described in this work represent the first examples of simultaneously displaying PF, DF, or RTP in different building blocks. These organic crystals reported here also exhibit interesting stimuli-responsive RTP properties and energy transfer process in heterojunction.[8] In addition, we demonstrated the utilization of a 3D printing technique to precisely control the location of molecular assemblies, creating a series of programable heterostructures with fluorescent and phosphorescent blocks (Figure 1d,e).

2. Results and Discussion

2.1. Chemical Structures and Photo-Physical Properties

In this work, a series of 1,3-dibutylphenanthro[9,10-d]imidazolium (compound **1**) and 1,3-di(4,4,4-trifluorobutyl)phenanthro[9,10-d]imidazolium cations (compound **2**) with different counteranions (I^-, PF_6^-, ClO_4^-, or BF_4^-) have been synthesized and characterized. Comprehensive synthetic details are summarized in Supporting Information. For compound **1I**, two types of single crystals were grown in CH_2Cl_2/hexene and CH_3CN/Et$_2$O, respectively, labeled as **1I-A** and **1I-B** (**Figure 2a**). For the crystal structure of **1I-A**, there are two types of dimers with π-π distances of 3.426 Å and 3.366 Å in the infinite chain. In comparison, the crystal structure of **1I-B** shows face-to-face dimers with intermolecular π-π distances of 3.464 Å and 3.421 Å, respectively (Figure 2a). For compound **2**, two co-crystals were grown and resolved by mixing **2I** with either **2ClO$_4$** (**2I+2ClO$_4$**) or **2BF$_4$** (**2I+2BF$_4$**), where X-ray diffraction analysis was used to determine the ratio between I^- and

**ADVANCED
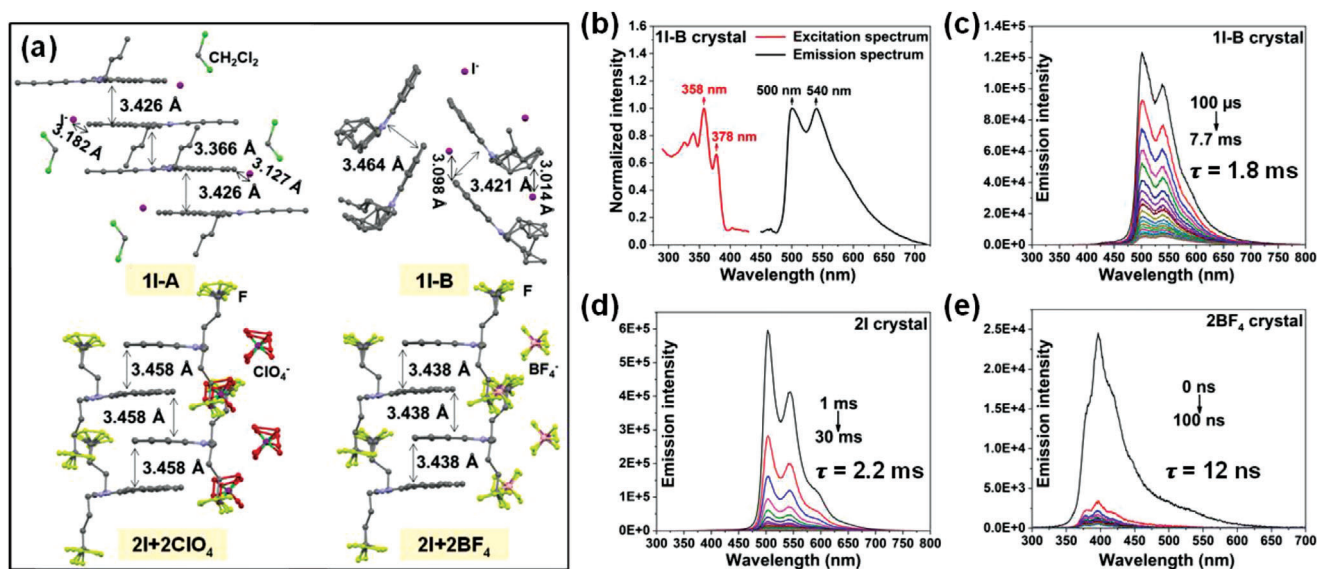SCIENCE NEWS**

www.advancedsciencenews.com

**ADVANCED
MATERIALS**

www.advmat.de

Figure 2. a) Single crystal structures of **1I-A**, **1I-B**, co-crystals **2I+2ClO₄** (2ClO₄:2I = 7:3) and **2I+2BF₄** (2BF₄:2I = 97:3), the ratio between I⁻ and ClO₄⁻/BF₄⁻ was determined by the X-ray diffraction analysis. b) Excitation and steady-state emission spectra of **1I-B** crystal. Time-resolved emission spectra of c) **1I-B**, d) **2I** and e) **2BF₄** crystal (λ_{ex} = 355 nm).

ClO₄⁻/BF₄⁻. The two co-crystals, **2I+2ClO₄** and **2I+2BF₄**, exhibit infinite π-π interactions in their chain structures, featuring π-π distances of 3.458 Å and 3.438 Å, respectively (Figure 2a).

The emission of pure crystals of **1I** and **2I** with I⁻ as counteranion exhibits a large Stokes shift and RTP with lifetimes in the millisecond time regime (Figure 2b–d). As shown in Figure 2b, the emission of crystal **1I-B** exhibits a significant Stokes shift of 0.8 eV, calculated from the energy difference between the absorption band at 378 nm and the emission band at 500 nm. This large Stokes shift indicates that the emission is phosphorescence in nature. The time-resolved emission spectra of **1I-B** and **2I** crystals were measured, as depicted in Figure 2c,d, showing their long emission lifetimes of 1.8 ms and 2.2 ms, respectively. Similarly, crystal **1I-A** exhibits the same RTP emission profile as crystals **1I-B** and **2I**, with an emission lifetime of 3 ms (Figure S1, Supporting Information). The emission spectra of **1I** and **2I** crystals exhibit two vibronic peaks at 500 nm and 540 nm, respectively, which are attributed to the $^3\pi\pi^*$ excited state.

This long-lived phosphorescence in the crystalline state disappears when the counteranions of compounds **1** and **2** crystals are changed from I⁻ to ClO₄⁻, PF₆⁻, or BF₄⁻. **1X** and **2X** (X = ClO₄⁻, PF₆⁻ or BF₄⁻) show blue prompt fluorescence with emission peaks at 380 and 400 nm and lifetimes in the nanosecond time regime (Figure 2e; Figure S2, Supporting Information). These results suggest that the I⁻ counteranion plays an important role in inducing solid-state long-lived RTP. The external heavy atom effect of I⁻ counteranion[9] is thought to turn on the RTP properties of compounds **1** and **2**. **1I-A** and **1I-B** crystals exhibit different phosphorescence emission quantum yields, which is 1% and 12% respectively. The distance between anions and cations is closer in **1I-B** crystal compared to **1I-A** (Figure 2a). The closer cation-anion distance is thought to enhance the external heavy atom effects and therefore increase the emission

(phosphorescence) quantum yield of **1I-B** crystal compared to **1I-A**.

Interestingly, the **2I+2ClO₄** and **2I+2BF₄** co-crystals exhibit multiple emission components of PF, DF, and RTP in the solid-state at room temperature (**Figures 3** and S3, Supporting Information). As shown in Figure 3a–c, for co-crystal of **2I+2ClO₄**, the respective time-resolved emission spectra collected from 0–360 ns, 1–12 µs, and 1–12 ms are characteristic of PF (emission lifetime of ≈10.3 ns), DF (emission lifetime of ≈2.1 µs) and RTP (emission lifetime of ≈2.8 ms). To study the effect of I⁻ doping on photo-physical properties, we mixed **2I** and **2BF₄** compounds in different ratios (from 1:2 to 2:98, n:n, I⁻:BF₄⁻) to obtain co-crystals. As shown in Figure 3d, by decreasing the doping ratio of I⁻ counteranions in the co-crystal, the relative intensity of phosphorescence to fluorescence decreases. This observation further points to the essential role of I⁻ counteranion in the RTP process.

According to the fluorescence and phosphorescence spectra, the energy difference between the S₁ and T₁ states of the co-crystal **2I+2ClO₄**/**2I+2BF₄** is calculated to be 0.8 eV. The large energy difference of 0.8 eV indicates that the DF does not originate from a TADF (thermally activated DF) process, which relies on a small $\Delta E_{S_1-T_1}$. The emission lifetimes of DF and RTP for these co-crystals do not show significant changes when the temperature changes, further indicating that the delayed emission does not originate from a thermally activated process (Figures S4 and S5, Supporting Information). The DF emission is attributed to a TTA process in the **2I+2ClO₄** co-crystal, which is based on the exciton-exciton interaction and exciton diffusion process in the solid state.[11] In co-crystals containing both I⁻ and ClO₄⁻ counteranions, triplet excitons are expected to be generated in the portion containing the I⁻ counteranion. Subsequently, the triplet exciton will diffuse into the portion containing the ClO₄⁻ counteranion.[10] Since the **2ClO₄** compound lacks an efficient T₁→S₀ radiative decay channel, subsequent exciton diffusion and TTA processes will take place in this portion, producing

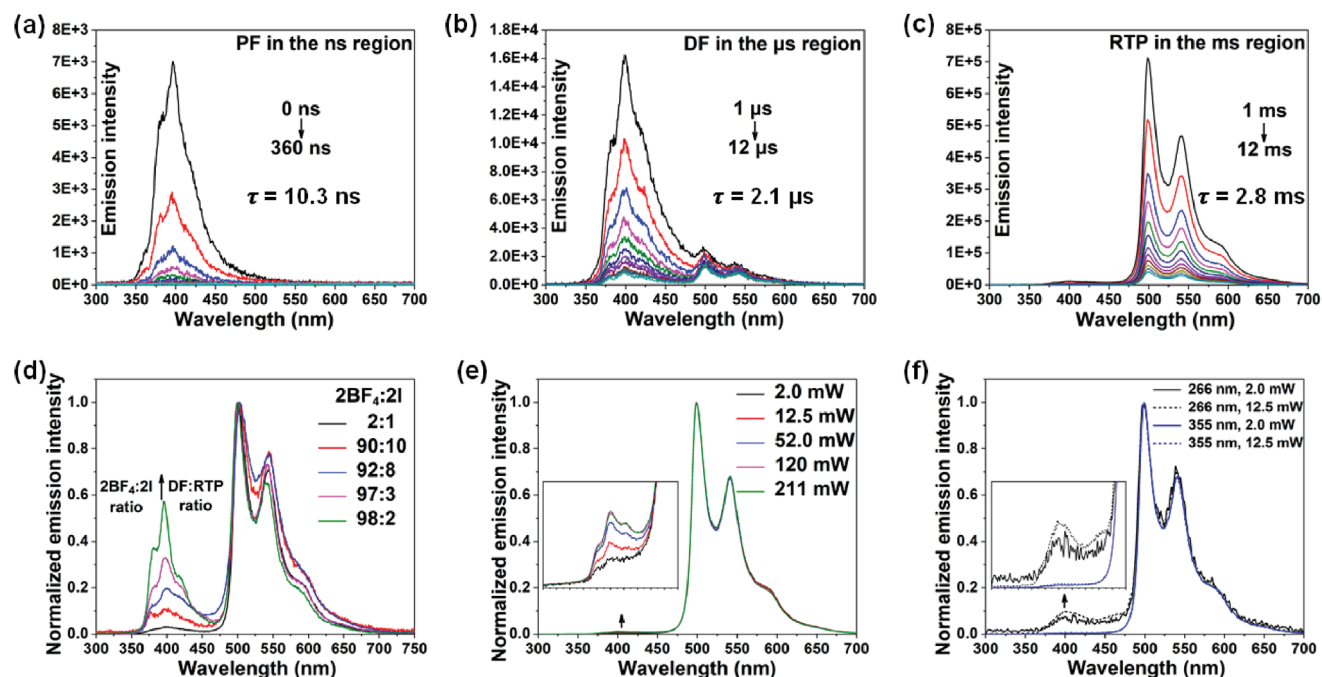**Figure 3.** Time-resolved emission spectra of **2I+2ClO₄** co-crystal from a) 0–360 ns, b) 1–12 μs and c) 1–12 ms (λ_{ex} = 355 nm). The doping ratio of I⁻ in the co-crystal is 30%. d) Normalized emission spectra of 2I+2BF4 co-crystals with different I− doping ratios recorded from 120 μs to 1 ms, showing DF and RTP components. Normalized emission spectra of 2I+2ClO4 co-crystals e) under different laser power excitation (λex = 355 nm) and f) under 266 nm and 355 nm laser excitation.

DF emission. The emission intensity of **2I+2BF₄** and **2I+2ClO₄** co-crystals was measured by changing the excitation laser intensity. As shown in Figure S6 (Supporting Information), we observed that the slope of $I_{em} \sim I_{ex}$ (emission intensity vs. excitation intensity) on the log scale is ≈0.5, showing that an effective TTA process occurs.[11]

The TTA process is highly dependent on the excitation power because high excitation power can generate more excitons and promote the exciton-exciton annihilation process. Therefore, we envision that the excitation power might be an external stimulus by which the relative fluorescence and RTP intensities of **2I+2ClO₄** and **2I+2BF₄** co-crystals can be adjusted. As shown in Figure 3e,f and Figure S7 (Supporting Information), the relative emission intensities of blue fluorescence and green phosphorescence in the co-crystals can be effectively modulated by changing the excitation power from 2 mW to 212 mW using a 355 nm excitation laser. Compared with phosphorescence, high-power laser excitation produces stronger fluorescence intensity. In addition, we found that the relative fluorescence and phosphorescence intensities could be further tuned by changing the wavelength of the excitation laser (266 or 355 nm). As shown in Figure 3f, by changing the laser excitation wavelength from 355 to 266 nm and keeping the excitation power at 2 mW, a larger fluorescence peak appeared in the co-crystal. As shown in Figure S8 (Supporting Information), the **2I+2BF₄** co-crystal has stronger absorptivity at 266 nm than at 355 nm, indicating that 266 nm laser excitation can produce excitons with higher concentration than 355 nm laser excitation at the same excitation laser power. A high exciton concentration in the solid state increases the probability of exciton-exciton annihilation and thus increases the DF intensity.

2.2. Fabrication and Characterization of Heterostructures

Based on these compounds with counteranion regulated emission properties (Figure S9, Supporting Information), we fabricated a series of heterostructures that individually emit PF, DF, or RTP in each corresponding block. As shown in the PXRD patterns (Figure S10, Supporting Information), **2I** and **2BF₄** compounds exhibit similar packing patterns in the crystalline states. This observation indicates lattice matching between these compounds and suggests that heterostructures can be fabricated. Through a step-by-step crystal growth approach (details in Experimental Section), we successfully fabricated multiblock hetero-architectures using compounds with I⁻, ClO₄⁻ and BF₄⁻ counteranions, as shown in **Figures 4** and S11 (Supporting Information). For the crystallization process, we first prepared pure micro-crystals of green-light emitting **2I** and blue-light emitting **2BF₄** (Figure S9). We used **2BF₄** micro-crystals as seeds to induce the growth of compound **2I**. As shown by the optical and confocal microscopy images in Figure 4, we obtained micron-sized tri-block heterostructures comprising a green phosphorescent **2I** shell and a blue fluorescent **2BF₄** core. We also used the initial **2I** micro-crystals as the seeds to induce the growth of **2I+2ClO₄** co-crystals, thus forming a heterostructure composed of **2I** (core) and **2I+2ClO₄** (shell) (Figure S11, Supporting Information). As shown in the fluorescent microscopy image in Figure S11a (Supporting Information), the inner core **2I** micro-crystal emits green phosphorescence, and the outer shell of **2I+2ClO₄** co-crystal emits DF, PF, and RTP simultaneously, showing aquamarine color.
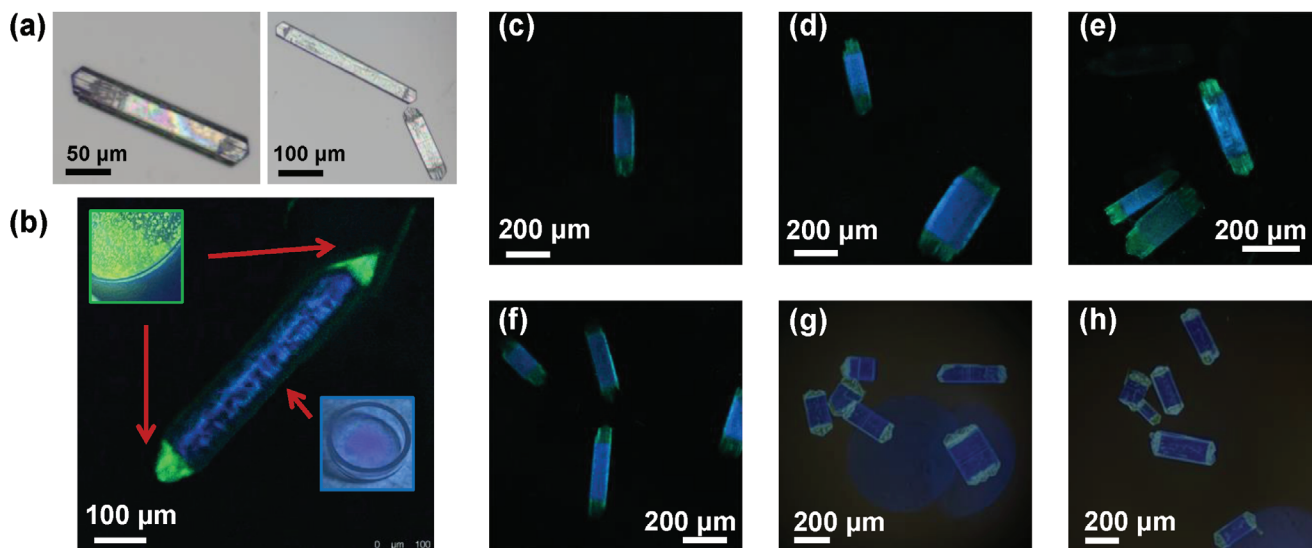
2402725 (4 of 8)

Figure 4. a) Optical images of **2BF₄** (core) and **2I** (shell) of the heterostructure **2BF₄@2I**. b–f) Confocal microscopy images of **2BF₄@2I** heterostructures excited by 405 nm laser. g,h) Fluorescent microscopy images of the **2BF₄@2I** heterostructures excited by 405 nm laser.

Next, we use time-resolved PL mapping technique to analyze the energy transfer process in the heterojunction part of the **2BF₄** (core) and **2I** (shell) heterostructures. Through wide-field excitation of different blocks (**Figure 5**a,b), we observed that the **2BF₄** core and **2I** shell have a short PL lifetime of ≈3.4 ns and a long-lived PL lifetime of ≈1.6 ms, respectively; the short PL lifetime is assigned to fluorescence and the long lifetime to phosphorescence. We then excited the blue-emitting block with a focused laser (Figure 5c, spot 1), and then recorded the PL images and PL decay kinetics (Figure 5d–f) at the excited location (Figure 5c, spot 1) as well as two additional sites (Figure 5c, spots 2 and 3). We used filters to obtain the PL images and PL decay kinet-

ics of the heterostructure with fluorescent blocks in the wavelength range 393–425 nm (PF) and phosphorescent blocks in the wavelength range 490–550 nm (RTP). As shown in the PL intensity changes in Figure 5d,e, the blue fluorescent emission gradually disappears in the heterojunction at x ≈40 μm, while the green phosphorescent emission increases significantly at the heterojunction (PL intensity in the red bracket of Figure 5e), indicating efficient blue-to-green emission energy transfer process. There are two possible mechanisms for the energy transfer process occurring at the heterojunction: (a) Upon laser excitation of the **2BF₄** core portion, singlet excitons are generated and diffuse into the heterojunction, with subsequent S_1(**2BF₄**)-T_1(**2I**) energy
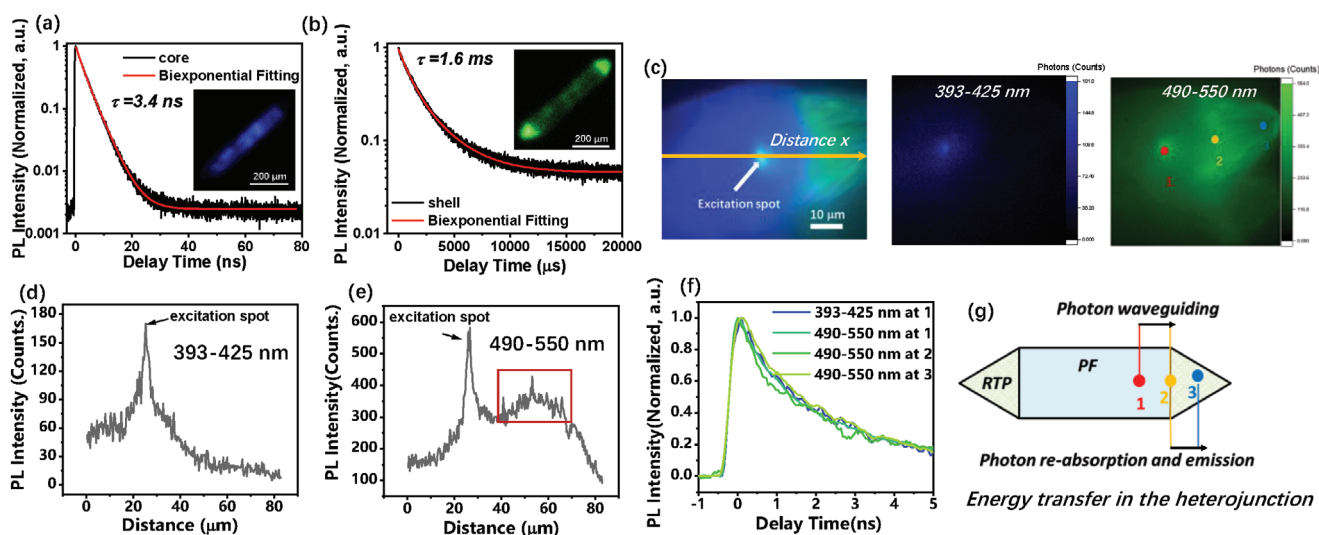

Figure 5. PL decay curve (black line) and the lifetime fitting curve (red line) of a) **2BF₄** (core) and b) **2I** (shell) in **2BF₄@2I** heterostructure (λ_{ex} = 375 nm). c) PL image of **2BF₄@2I** heterostructures (λ_{ex} = 375 nm). The variation in PL intensity along the x-axis (see panel c) for the d) fluorescent (393-425 nm) and e) phosphorescent (490–550 nm) components. f) Comparison of PL dynamics at spots 1, 2, and 3 (see panel c) of the **2BF4@2I** heterostructure. g) Schematic showing the energy transfer process in the heterojunction of the **2BF4@2I** heterostructures.
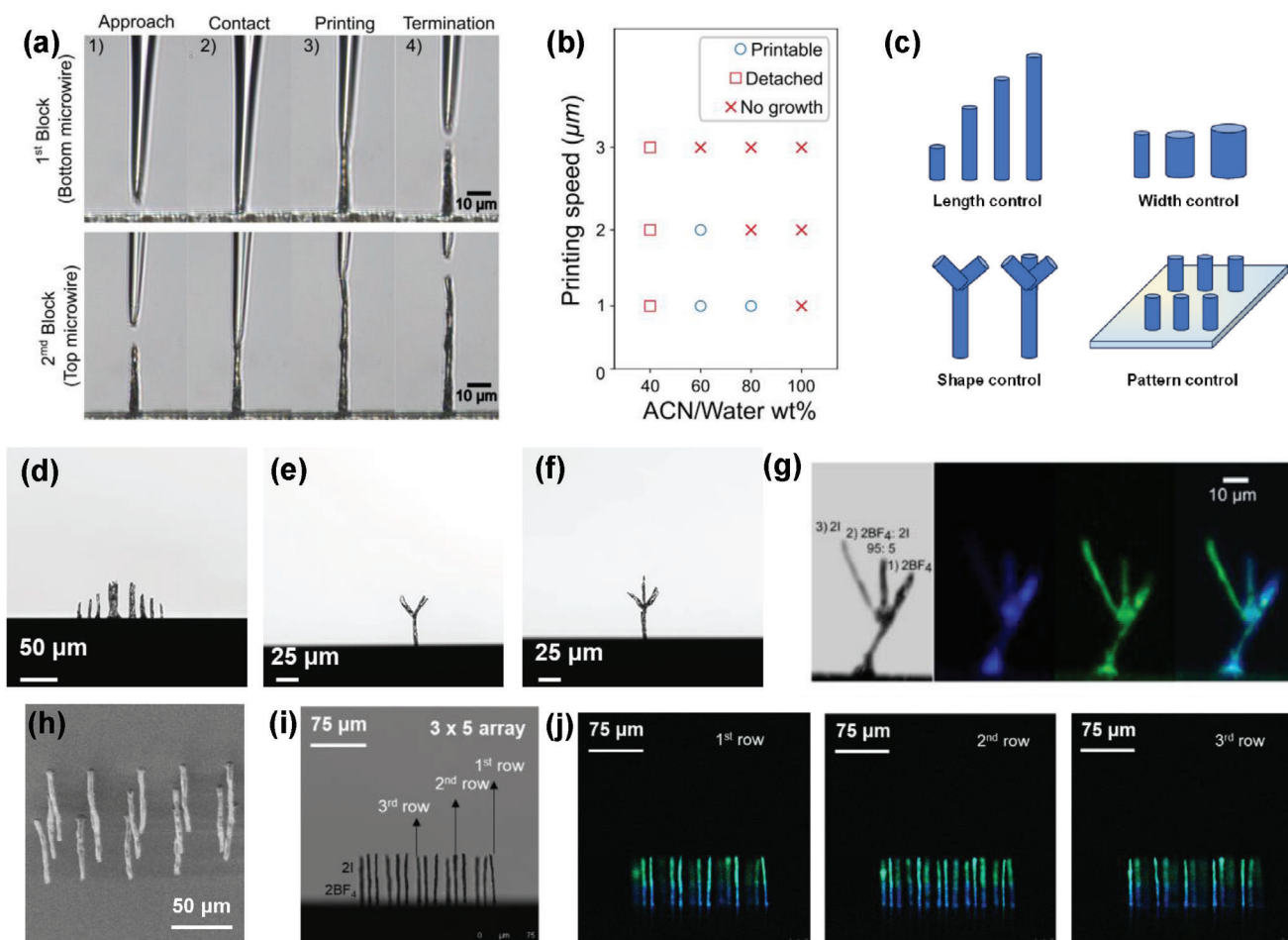
**ADVANCED
SCIENCE NEWS**

www.advancedsciencenews.com

**ADVANCED
MATERIALS**

www.advmat.de

Figure 6. a) Optical microscopy images of the two-step printing process for **2BF₄** (bottom) and **2I** (top) diblock heterostructure. b) Printability chart depending on printing speed and acetonitrile concentration. c) Schematic illustration of the length-, width-, shape-, and array pattern-controlled microstructures prepared using a 3D printing technique. d–g) Optical and confocal images of printed micro-wires with controlled length, width, shape, and pattern made from compound **2I**, **2BF₄**, and **2I+2BF₄**. h) SEM, i) optical, and j) confocal images of 3 × 5 heterostructure arrays printed using compounds **2I** (top) and **2BF₄** (bottom). The image j of samples at different rows was recorded by adjusting the focal plane of the microscope.

transfer process that results in blue-to-green emission energy transfer.[1a] (b) Singlet excitons in **2BF₄** crystal lead to a blue light emission. Blue light propagates at the crystal interface through the optical waveguide effect, which is achieved through light reflection. Then, a reabsorption process occurs at the **2BF₄**-**2I** heterojunction, where the green **2I** crystal reabsorbs the blue light and subsequently emits low-energy green phosphorescence.[3] To differentiate these two mechanisms, we recorded and compared the PL kinetics obtained at spots 1, 2, and 3 by exciting spot 1. As shown in Figure 5f, the rising edge of the PL dynamics of the shell (spot 3) does not appear any time delay compared to the PL dynamics recorded by the body (spot 1) excitation. This suggests that the energy transfer process from fluorescent block to the phosphorescent block is due to the waveguide effect (mechanism **b**) and the process is close to the speed of light. The fast PL decay observed at spots 2 and 3 in Figure 5f is attributed to the waveguided fluorescence of the **2BF₄** core, which has a minor contribution in the emission range of 490-520 nm (Figure 3a). Figure 5g depicts a mechanistic schematic of the energy transfer process in the heterojunction of the **2BF₄@2I** heterostructure.

2.3. 3D Printing

The ability to construct complex microstructures at designated positions is crucial for the development of future high-performance photonic circuits. Herein, we further demonstrate the sequential 3D printing of microscale heterostructures composed of **2BF₄**, **2I** crystals, and **2BF₄+2I** co-crystals by utilizing the rapid evaporation of solvent in the femtoliter volume-limited meniscus without adding additives.

Figure 6a shows the corresponding snapshot during the printing process taken from the recorded video (Video S1, Supporting Information). We used borosilicate micro nozzles (controlled size of 1 to 8 μm diameter) prepared by thermal-pulling (thermal heating and pulling) as a reservoir and carrier (Figure 6a1). A meniscus is formed when the micro nozzle contacts the glass substrate (Figure 6a2). During the movement of the micro nozzle, the rapid evaporation of the solvent within the confined space enables the printing of free-form structures without the help of additives (Figure 6a3). The micro nozzle abruptly moves at a speed of 500 μm s⁻¹, momentarily terminating the printing process

**ADVANCED
SCIENCE NEWS**

www.advancedsciencenews.com

**ADVANCED
MATERIALS**

www.advmat.de

(Figure 6a4). The printed diblock microwires shown in Figure 6a are composed of **2BF$_4$** at the bottom and **2I** at the top, respectively.

Control of solution wetting and printing speed is a prerequisite for reliable multi-step printing of heterostructures. We checked the printability of the solution based on the solvent composition and printing speed (Figure 6b). Stable printing is achieved under specific conditions (O). However, when using 40:60% (v/v) acetonitrile-water solution, the grown microstructure detached from the surface as the micro nozzle moved, as shown in Figure S12 (Supporting Information). On the other hand, when acetonitrile was used as a single solvent, it was found that the printing process was unable, presumably because the wetting (X) of acetonitrile solvent was too large to form solidified structure in the micro nozzle-confined space. We hypothesize that the wetting of the prepared solution on the substrate and the supersaturation of the solution in the meniscus determine the printability, as summarized (Figures S13 and S14, Supporting Information).

Our technique enables precise control over the length, width, shape, and array patterns (Figure 6c). We demonstrate printing with controlled lengths ranging from 20 to 40 μm and widths ranging from 1 to 8 μm (Figure 6d; Figure S15, Supporting Information). In addition, the programed branched structures (Figure 6e–g) and 3 × 5 diblock heterostructure arrays (Figure 6h,i) demonstrate the feasibility of 3D printing to construct complex structures and patterns. Under confocal microscope, the printed heterostructures in a 3 × 5 array showed blue emission from the bottom **2BF$_4$** crystals and green emission from the top **2I** crystals (Figure 6j; Video S3, Supporting Information). The **2I** and **2BF$_4$** blocks in the printed heterostructures were further characterized by the Transmission Electron Microscope (TEM) images and corresponding Selected Area Electron Diffraction (SAED) patterns, as shown in Figure S16 (Supporting Information). The planes of SAED patterns were carefully indexed based on the obtained d-spacing and PXRD results. The color mixing in Figure 6g,j is believed to occur due to the diffusion process of molecules (**2I**) when the micro nozzle containing the solution comes into contact with the printed **2BF$_4$** block. The heterostructure fabricated using self-assembly methods and 3D printing techniques exhibits waveguided light (Figure S17, Supporting Information), with sub 100 nm surface roughness, as shown in Figures S18 and S19 (Supporting Information), highlighting its application potential in the field of integrated optical waveguides.

3. Conclusion

In summary, we achieved PF, DF, and RTP in metal-free organic crystals by modulating the counteranions of a series of imidazole cationic molecules. The relative intensity between the fluorescent and phosphorescent emission components can be manipulated by external stimuli, including the power and wavelength of the laser excitation. A series of heterostructures based on these organic cations have been fabricated through controllable crystallization-driven self-assembly method or 3D printing technique. These heterostructures display PF, DF, or RTP in different building blocks, where efficient energy transfer processes in the heterojunction are probed. We expect these findings to expand the potential and practical applicability of molecular heterostructured materials.

Table 1. Fitting parameters of the PL kinetics shown in Figure 5a (core) and 5b (shell).

	$\tau_1[A_1]$	$\tau_2[A_2]$
core	1.80 ns [0.28]	4.05 ns [0.72]
shell	1.01 ms [0.59]	2.81 ms [0.41]

4. Experimental Section

Synthesis of Compound 1 and 2: All starting materials were purchased from commercial sources and used as received. Unless otherwise stated, the solvents used for the synthesis were of analytical grade. Electrospray Ionization (ESI) mass spectra were obtained on a Bruker maXis II high resolution Q-TOF mass spectrometer (samples were dissolved in HPLC grade acetonitrile). NMR spectra were measured at 298 K on a Bruker DPX-500 or DPX-400 spectrometer. Elemental analyses were performed at the Institute of Chemistry, Chinese Academy of Sciences, Beijing. All reactions were performed under air atmosphere unless otherwise stated. Detailed experimental procedures and characterizations of the samples are provided in Supporting Information.

Preparation of Multiblock Heterostructures: The core-shell heteroarchitecture structures were named as **2BF$_4$@2I** (core: **2BF$_4$**, shell: **2I**,) and **2I@2I+2ClO$_4$** (core: **2I**, shell: **2I+2ClO$_4$**), respectively.

Seed preparation of 2BF$_4$ and 2I: the blue-emitting **2BF$_4$** and green-emitting **2I** seeds (core part) were prepared by slowly diffusing diethyl ether vapor into concentrated DMF solutions of **2BF$_4$** and **2I**, respectively. Micro-seeds of **2BF$_4$** and **2I** were obtained after the process of washing and ultra-sonication.

Suspension Preparation of 2I and 2I+2ClO$_4$: The **2I** or **2I+2ClO$_4$** solution was prepared by dissolving **2I** or **2I+2ClO$_4$** (5mg) into 2 mL of CH$_3$CN, respectively. A cloudy suspension was then obtained by adding 0.5 mL of H$_2$O (poor solvent) into their respective CH$_3$CN solution.

Preparation of the Heterostructures: The dried **2BF$_4$** and **2I** crystalline seeds were added to suspensions containing **2I** and **2I+2ClO$_4$**, respectively. The suspensions were then left to stand at room temperature for two days. During this time, the shell blocks gradually grew at both ends of the micro-crystal core, resulting in the formation of a core-shell heterostructure.

Time-Resolved Photoluminescence (PL) Spectrum Measurements: PL measurements were performed on a home-made PL-scanning imaging microscope equipped with a time-correlated single photon counting (TCSPC) module. For focused illumination imaging measurements, the excitation laser beam was focused on the sample at 375 nm wavelength (PDL 800-B, PicoQuant, Germany) through a 100 × air objective lens (NA = 0.95, Olympus PLFLN 100 ×). By parking the excitation laser spot at a specific position, rapid scanning of the galvanometer mirror ensured that photons emitted from the entire crystal were collected. For wide-field illumination PL imaging measurements, the excitation laser beam was un-collimated in front of a 10 × (NA = 0.4) objective lens to form a uniform excitation spot to excite the entire crystal. Each scanned image contained 256 × 256 pixels. Fluorescent signals were collected using two high speed detectors (HPM-100-50 and HPM-100-40, Hamamatsu, Japan). Band pass filters 393–425 nm were selected for PF and 490–550 nm for RTP PL collection.

The PL kinetics in Figure 5a,b were both fitted by a biexponential decay function in the form of $I = A_1 * \exp(-\frac{t}{\tau_1}) + A_2 * \exp(-\frac{t}{\tau_2})$. Then the averaged PL lifetime was calculated by $\tau_{Ave} = (A_1*\tau_1 + A_2*\tau_2)/(A_1 + A_2)$. The fitting parameter was listed in **Table 1**.

3D Printing Methods: 3D printing of freestanding of **2BF$_4$** and **2I** heterostructures was performed on glass substrate at room temperature, 40% RH (relative humidity), using a home-built 3D printing platform. **2BF$_4$** or **2I** at a concentration of 1.5 mg mL^{-1} in various acetonitrile-water mixtures was used as solution link. Figure 1d shows a schematic

**ADVANCED
SCIENCE NEWS**

www.advancedsciencenews.com

**ADVANCED
MATERIALS**

www.advmat.de

diagram of the 3D printing platform. Heat-pulled borosilicate micro nozzles were used as reservoirs and carriers for the solutions required to print heterostructures. A motorized stage (resolution: 100 nm) precisely positioned the micro nozzle and substrate at specified x-, y-, and z-axis coordinates. A charge-coupled device (CCD) camera attached to a 50 × objective lens aligned with light illuminating the substrate in parallel provided real-time images, enabling sequential printing of heterogeneous organic crystal structures.

Borosilicate glass micro nozzles with different diameters (1 to 8 μm) were fabricated using a commercialized heat-pulling machine (P-97, Sutter Instruments). Custom software controlled the assembled motorized stages (Khouzu precision) to move the solution-filled micro nozzles and the substrate to the desired position at specified speeds to perform the 3D printing process. A CCD camera (Blackfly, Teledyne FLIR) attached to a 50 × infinity-corrected objective lens (NA = 0.55, Mitutoyo) allowed observation and recording of the printing process.

Conflict of Interest

The authors declare no conflict of interest.

Data Availability Statement

The data that support the findings of this study are available from the corresponding author upon reasonable request.

[1] a) M.-J. Sun, Y. Liu, Y. Yan, R. Li, Q. Shi, Y. S. Zhao, Y.-W. Zhong, *J. Am. Chem. Soc.* **2018**, *140*, 4269; b) M.-P. Zhuo, J.-J. Wu, X.-D. Wang, Y.-C. Tao, Y. Yuan, L.-S. Liao, *Nat. Commun.* **2019**, *10*, 3839; c) A. Dodabalapur, H. E. Katz, L. Torsi, R. C. Haddon, *Science* **1995**, *269*, 1560.

[2] a) Y. Lei, Q. Liao, H. Fu, J. Yao, *J. Am. Chem. Soc.* **2010**, *132*, 1742; b) Q. Kong, Q. Liao, Z. Xu, X. Wang, J. Yao, H. Fu, *J. Am. Chem. Soc.* **2014**, *136*, 2382; c) M.-J. Sun, Y. Liu, W. Zeng, Y. S. Zhao, Y.-W. Zhong, J. Yao, *J. Am. Chem. Soc.* **2019**, *141*, 6157; d) J. Y. Zheng, Y. Yan, X. Wang, Y. S. Zhao, J. Huang, J. Yao, *J. Am. Chem. Soc.* **2012**, *134*, 2880; e) Z.-Z. Li, J.-J. Wu, X.-D. Wang, K.-L. Wang, S. Zhang, W.-F. Xie, L.-S. Liao, *Adv. Opt. Mater.* **2019**, *7*, 1900373; f) R. Huang, C. Wang, Y. Wang, H. Zhang, *Adv. Mater.* **2018**, *30*, 1800814; g) C. Zhang, Y. Yan, J. Yao, Y. S. Zhao, *Adv. Mater.* **2013**, *25*, 2854.

[3] Q. Wan, K. Xiao, Z. Li, J. Yang, J. T. Kim, X. Cui, C.-M. Che, *Adv. Mater.* **2022**, *34*, 2204839.

[4] S. Ogi, K. Sugiyasu, S. Manna, S. Samitsu, M. Takeuchi, *Nat. Chem.* **2014**, *6*, 188.

[5] J. B. Gilroy, T. Gädt, G. R. Whittell, L. Chabanne, J. M. Mitchels, R. M. Richardson, M. A. Winnik, I. Manners, *Nat. Chem.* **2010**, *2*, 566.

[6] a) Z. An, C. Zheng, Y. Tao, R. Chen, H. Shi, T. Chen, Z. Wang, H. Li, R. Deng, X. Liu, W. Huang, *Nat. Mater.* **2015**, *14*, 685; b) S. Hirata, *Appl. Phys. Rev.* **2022**, *9*, 011304; c) W. Zhao, Z. He, B. Z. Tang, *Nat. Rev. Mater.* **2020**, *5*, 869; d) Q. Peng, Y. Yi, Z. Shuai, J. Shao, *J. Am. Chem. Soc.* **2007**, *129*, 9333; e) X.-F. Wang, H. Xiao, P.-Z. Chen, Q.-Z. Yang, B. Chen, C.-H. Tung, Y.-Z. Chen, L.-Z. Wu, *J. Am. Chem. Soc.* **2019**, *141*, 5045; f) R. Kabe, C. Adachi, *Nature* **2017**, *550*, 384; g) P. Alam, T. S. Cheung, N. L. C. Leung, J. Zhang, J. Guo, L. Du, R. T. K. Kwok, J. W. Y. Lam, Z. Zeng, D. L. Phillips, H. H. Y. Sung, I. D. Williams, B. Z. Tang, *J. Am. Chem. Soc.* **2022**, *144*, 3050.

[7] a) X. Wang, H. Shi, H. Ma, W. Ye, L. Song, J. Zan, X. Yao, X. Ou, G. Yang, Z. Zhao, M. Singh, C. Lin, H. Wang, W. Jia, Q. Wang, J. Zhi, C. Dong, X. Jiang, Y. Tang, X. Xie, Y. Yang, J. Wang, Q. Chen, Y. Wang, H. Yang, G. Zhang, Z. An, X. Liu, W. Huang, *Nat. Photonics* **2021**, *15*, 187; b) W. Ye, H. Ma, H. Shi, H. Wang, A. Lv, L. Bian, M. Zhang, C. Ma, K. Ling, M. Gu, Y. Mao, X. Yao, C. Gao, K. Shen, W. Jia, J. Zhi, S. Cai, Z. Song, J. Li, Y. Zhang, S. Lu, K. Liu, C. Dong, Q. Wang, Y. Zhou, W. Yao, Y. Zhang, H. Zhang, Z. Zhang, X. Hang, et al., *Nat. Mater.* **2021**, *20*, 1539; c) X.-F. Wang, W.-J. Guo, H. Xiao, Q.-Z. Yang, B. Chen, Y.-Z. Chen, C.-H. Tung, L.-Z. Wu, *Adv. Funct. Mater.* **2020**, *30*, 1907282; d) C. Chen, Z. Chi, K. C. Chong, A. S. Batsanov, Z. Yang, Z. Mao, Z. Yang, B. Liu, *Nat. Mater.* **2021**, *20*, 175; e) B. Ding, L. Ma, Z. Huang, X. Ma, H. Tian, *Sci. Adv.* **2021**, *7*, eabf9668; f) N. Notsuka, R. Kabe, K. Goushi, C. Adachi, *Adv. Funct. Mater.* **2017**, *27*, 1703902; g) X. Wang, Y. Sun, G. Wang, J. Li, X. Li, K. Zhang, *Angew. Chem., Int. Ed.* **2021**, *60*, 17138; h) Q. Peng, H. Ma, Z. Shuai, *Acc. Chem. Res.* **2021**, *54*, 940; i) F. Xiao, M. Wang, Y. Lei, W. Dai, Y. Zhou, M. Liu, W. Gao, X. Huang, H. Wu, *J. Mater. Chem. C* **2020**, *8*, 17410; j) C.-R. Wang, Y.-Y. Gong, W.-Z. Yuan, Y.-M. Zhang, *Chin. Chem. Lett.* **2016**, *27*, 1184.

[8] a) H. Shi, W. Yao, W. Ye, H. Ma, W. Huang, Z. An, *Acc. Chem. Res.* **2022**, *55*, 3445; b) L. Gu, H. Shi, M. Gu, K. Ling, H. Ma, S. Cai, L. Song, C. Ma, H. Li, G. Xing, X. Hang, J. Li, Y. Gao, W. Yao, Z. Shuai, Z. An, X. Liu, W. Huang, *Angew. Chem., Int. Ed.* **2018**, *57*, 8425; c) Z. Man, Z. Lv, Z. Xu, M. Liu, J. He, Q. Liao, J. Yao, Q. Peng, H. Fu, *J. Am. Chem. Soc.* **2022**, *144*, 12652.

[9] a) S. P. McGlynn, T. Azumi, M. Kasha, *J. Chem. Phys.* **1964**, *40*, 507; b) Q. Wan, W.-P. To, X. Chang, C.-M. Che, *Chem* **2020**, *6*, 945; c) S. P. McGlynn, R. Sunseri, N. Christodouleas, *J. Chem. Phys.* **1962**, *37*, 1818; d) O. Bolton, K. Lee, H.-J. Kim, K. Y. Lin, J. Kim, *Nat. Chem.* **2011**, *3*, 205.

[10] O. V. Mikhnenko, P. W. M. Blom, T.-Q. Nguyen, *Energy Environ. Sci.* **2015**, *8*, 1867.

[11] a) C. Bohne, E. B. Abuin, J. C. Scaiano, *J. Am. Chem. Soc.* **1990**, *112*, 4226; b) Q. Wan, D. Li, J. Zou, T. Yan, R. Zhu, K. Xiao, S. Yue, X. Cui, Y. Weng, C.-M. Che, *Angew. Chem., Int. Ed.* **2021**, *61*, 202114323.